



A coupled meshfree/finite element method for automotive crashworthiness simulations

Hui-Ping Wang^{a,*}, Cheng-Tang Wu^b, Yong Guo^b, Mark E. Botkin^a

^a GM Research and Development Center, Mail Code 480-106-256, 30500 Mound Road, Warren, MI 48090-9055, USA

^b Livermore Software Technology Corporation, 7374 as Positas Road, Livermore, CA 94550, USA

ARTICLE INFO

Article history:

Received 30 October 2008

Received in revised form

18 February 2009

Accepted 2 March 2009

Available online 21 March 2009

Keywords:

Meshfree method

Element free Galerkin method

Finite element method

Offset deformable barrier

Crashworthiness simulation

ABSTRACT

Mesh distortion induced numerical instability is a major roadblock in automotive crashworthiness finite element simulations. Remedies such as wrapping elements with null shells and deletion of distorted meshes have been adopted but none of them seems robust enough to survive various scenarios. Meshfree methods have been developed over the past almost twenty years in view of their capabilities in dealing with large material deformation and separation, but have remained in academic research due to their unaffordable high computational cost in solving large-scale industrial applications. This paper presents a coupled meshfree/finite-element method which allows engineers to model the severe deformation area with the meshfree method while keeping the remaining area modeled by the finite element methods. The method is implemented into LS-DYNA version 971 and its later versions so that it is available for automotive crashworthiness simulations. In the paper, one linear patch test and three crash examples are presented to demonstrate the accuracy of the meshfree formulation, its effectiveness in resolving mesh distortion difficulty, and the efficiency of the coupled meshfree/finite element solver in handling large-scale models.

© 2009 Elsevier Ltd. All rights reserved.

1. Introduction

Today's vehicle development process heavily relies on computer-aided engineering (CAE) analysis. In most scenarios, the CAE analysis provides quick and accurate assessment of newly designed vehicle components and systems in terms of their manufacturability and targeted performance. Also, the analysis helps to improve the design by virtually optimizing design parameters to achieve the design target at best. With the usage of the CAE analysis, the amount of expensive and time-consuming physical tests is greatly reduced nowadays. Still, there are scenarios current CAE technologies cannot well comprehend. Exemplary problems are events and processes involving severe deformation, material separation, fluid–solid interaction, phase changing and other complex physics.

One of the obstacles limiting current CAE tools' capability is the mesh quality problem. The finite element (FE) method employed in the CAE tools models the physical domain with discrete, non-overlapping conforming meshes. The order of the finite element approximation being constructed at each element degenerates

when the element has high aspect-ratio or geometric distortion. Consequently, the accuracy of the FE-based CAE analysis degrades. Sometimes the analysis even fails. This often occurs in the simulations involving severe deformation or large shape change such as in the numerical modeling of vehicle crash events. A good exemplary problem is the frontal Offset Deformable Barrier (ODB) model. The ODB is used in Insurance Institute for Highway Safety (IIHS) 40MPH Frontal Offset Crash Test and European New Car Assessment Program (Euro NCAP) 64KPH (40MPH) Frontal Offset Crash Test. As shown in Fig. 1, the honeycomb barrier is severely compressed in the physical frontal offset impact test [1]. In its corresponding virtual crash simulation, the mesh-based ODB model undergoes the same amount of large deformation, which often results in severe mesh distortion in the model and causes solid elements to have negative element volume. The finite element analysis stops when the negative element volume is detected. The negative element volume is not only non-physical but also violates basic conditions on motion in the finite element theory, that is, the determinant of deformation gradient cannot be negative. Even if the analysis continues, the accumulated approximation error due to the mesh distortion usually leads the analysis to an inaccurate solution. Many remedies have been adopted to resolve the distortion problem. One popular approach is to wrap each element with null shells and specify contact constraints among these null shells

* Corresponding author. Tel.: +86 21 2898 7319; fax: +86 21 5840 6291.

E-mail address: hui-ping.wang@gm.com (H.-P. Wang).



Fig. 1. Post-test offset deformable barrier (after Mayer et al. [1]).

to prevent any inverted elements. This not only introduces artificial stiffness into the system and therefore pollutes the solution accuracy but also adds computational effort into the analysis. The second common approach is simply to delete the distorted meshes from the model. This method can only be practiced when the number of distorted elements in the parts is relatively small and the damage to the solution accuracy due to the deletion is negligible. The third frequent approach is to re-mesh the problematic area carefully to avoid any fatal distortion, which is a trial-and-error approach since under large deformation no mesh is bulletproof. In summary, to date there is no single approach which is viable enough to survive various virtual crash simulation scenarios.

Meshfree methods have been proposed and developed to resolve this mesh-distortion difficulty since the 1990s due to their 'meshfree' characteristic. Typical meshfree methods are Element Free Galerkin (EFG) Method, Reproducing Kernel Particle Method, HP-clouds method and Partition of Unity method [2–7]. The common feature of these methods is their ability to construct their approximation functions at discrete points of a domain without usage of element connectivity among the discrete points. The approximation functions are applied in interpolating domain variables so that the corresponding math problems can be solved. Representative meshfree approximations are moving least squares approximation and reproducing kernel approximation. These approximation functions can have high order smoothness if needed, therefore are able to exactly approximate functions of high order monomials. Applications of these approximations in solving nonlinear large deformation or material separation problems [5,8,9,17] have shown their great advantages over the conventional FE methods in terms of model adaptivity and solution accuracy. However, the meshfree methods consume much higher CPU time than the FE methods, which greatly limits their applications in solving large-scale industrial problems. A complete review on meshfree methods can be found in [21].

The idea of coupling the meshfree method with the existing FE methods was originally proposed by meshfree researchers for the purpose of imposing essential boundary conditions in meshfree computations as shown in [10–13]. Nevertheless, it started the idea of patching the meshfree formulation with the FE formulation within one model. The coupling allows the meshfree method to be applied only to the area where the meshfree method is needed

while the low-cost FE method is used for the remainder of the model. In this way, the meshfree method can be used in solving large-scale problems without big CPU penalty, since in most cases large deformation or material separation only occurs at a locally confined area which is relatively small compared to the overall model. A more general review on several coupling methods was given in [18]. The major challenge in the coupling is to maintain the desired order of continuity across the meshfree and FE zones, and have the overall approximation to meet desired consistency conditions. Various mixed formulations [10,11,13,19,20] were proposed but none of them was fully developed for industrial applications.

In this paper, a novel coupled meshfree/FE method is presented. It is intended for large-scale explicit dynamic simulations. The EFG method is employed in the meshfree formulation. The approximation functions along the interfaces between the meshfree and FE zones are designed to ensure the first-order continuity in the approximations across the interfaces and meet the first-order consistency condition. Section 2 of the paper reviews the Moving Least Squares approximation used in the EFG method. Section 3 presents the proposed coupled meshfree/finite element formulation for three-dimensional explicit dynamic problems, followed in Section 4 by a linear patch test and three numerical examples. Conclusions are drawn in Section 5.

2. Meshfree approximation

2.1. Moving Least Squares approximation

The Moving Least Squares (MLS) approximation [2,3] is used to construct the shape function in the EFG method. Let \mathbf{u} be a function defined on a domain Ω , and let the domain Ω be discretized by a set of points $\{\mathbf{X}_I\}_{I=1}^{NP} \subset \Omega$. The MLS approximation of the function $\mathbf{u}(\mathbf{X})$, denoted by $\mathbf{u}^h(\mathbf{X})$, is

$$\mathbf{u}^h(\mathbf{X}) = \sum_{j=1}^n b_j h_j(\mathbf{X}) = \mathbf{h}^{[n]}(\mathbf{X}) \mathbf{b}^{[n]} \quad (1)$$

where $\mathbf{h}^{[n]}(\mathbf{X}) = (1, X, Y, Z, X^2, \dots, Z^n)^T$ is the vector of a monomial basis in the coordinates $\mathbf{X}^T = [X, Y, Z]$ so that the basis is complete and n is the order of the monomial. The coefficients b_j , $j = 1, 2, \dots, n$ are solved by minimizing the following weighted, discrete L_2 norm:

$$\mathbf{E}(b_j) = \sum_{I=1}^{NP} \Phi_a(\mathbf{X} - \mathbf{X}_I) \left(\sum_{j=1}^n b_j h_j(\mathbf{X}_I) - \mathbf{u}(\mathbf{X}_I) \right)^2 \quad (2)$$

$\Phi_a(\mathbf{X} - \mathbf{X}_I)$ is a weight function which associates to each point and has a compact support 'a'. When $\partial \mathbf{E}(b_j) / \partial b_j = 0$, the coefficients b_j are solved as

$$\mathbf{b}^{[n]}(\mathbf{X}) = \sum_{I=1}^{NP} \Phi_a(\mathbf{X} - \mathbf{X}_I) \mathbf{M}^{[n]-1}(\mathbf{X}) \mathbf{h}^{[n]}(\mathbf{X}_I) \mathbf{u}(\mathbf{X}_I); \quad (3)$$

$$\mathbf{M}^{[n]}(\mathbf{X}) = \sum_{J=1}^{NP} \Phi_a(\mathbf{X} - \mathbf{X}_J) \mathbf{h}^{[n]}(\mathbf{X}_J) \mathbf{h}^{[n]T}(\mathbf{X}_J) \quad (4)$$

assuming $\mathbf{M}^{[n]}(\mathbf{X})$ is non-singular. For the case $n = 1$, a sufficient condition for a non-singular $\mathbf{M}^{[1]}(\mathbf{X})$ is that \mathbf{X} for $\mathbf{X} \in \Omega$ is at least covered by the supports of four weight functions $\Phi_a(\mathbf{X} - \mathbf{X}_J)$, $J = 1, 2, 3, 4$, where $\mathbf{X}_1, \mathbf{X}_2, \mathbf{X}_3$ and \mathbf{X}_4 are not on the same plane in the three dimensional problem. Substituting Eq. (3) into Eq. (1), we have the MLS interpolant expressed as

$$\mathbf{u}^h(\mathbf{X}) = \sum_{I=1}^{NP} \psi_I^{[n]}(\mathbf{X}; \mathbf{X} - \mathbf{X}_I) \mathbf{u}(\mathbf{X}_I) \quad (5)$$

$$\psi_I^{[n]}(\mathbf{X}; \mathbf{X} - \mathbf{X}_I) = \phi_a(\mathbf{X} - \mathbf{X}_I) \mathbf{h}^{[n]T}(\mathbf{X}) \mathbf{M}^{[n]-1}(\mathbf{X}) \mathbf{h}^{[n]}(\mathbf{X}_I) \quad (6)$$

where $\psi_I^{[n]}(\mathbf{X}; \mathbf{X} - \mathbf{X}_I)$ is the MLS shape function.

Fig. 2 is an example of a MLS shape function constructed using a cubic B-spline weight function and a linear basis. The employment of the MLS shape functions in the Galerkin approximation of a partial differential equation is called the EFG method.

Notice that $\psi_I^{[n]}(\mathbf{X}; \mathbf{X} - \mathbf{X}_I)$ in Eq. (6) is generally not an interpolation function, that is, the MLS shape functions do not have Kronecker delta properties and $\mathbf{u}^h(\mathbf{X}_I)$ may not be equal to $\mathbf{u}(\mathbf{X}_I)$ in Eq. (5). Each $\mathbf{u}^h(\mathbf{X}_I)$ is calculated from the coefficients $\mathbf{u}(\mathbf{X}_I)$, $I = 1, 2, \dots, NP$ using Eq. (5), which is more cumbersome compared to the finite element method. Because of this lack of Kronecker delta property, special treatments are necessary in enforcing essential boundary conditions when the MLS shape functions are used to approximate boundary value problems [14]. Also, the resulting stiffness matrix for the linear system of algebraic equation after these treatments is usually neither banded nor sparse; therefore the solution of the linear system becomes expensive. This is especially obvious in an implicit computation.

3. Coupled meshfree/finite element method

The purpose of coupling the meshfree method and the FE method is to keep the computational cost due to the meshfree modeling low so that the problems can be solved at a cost as low as possible. Fig. 3 illustrates the main concept of this coupling. The problem domain Ω is divided into FE sub-domains and meshfree sub-domains, that is, $\Omega = \Omega_{FEM} \cup \Omega_{meshfree}$. The FE sub-domains consist of non-overlapping and conforming elements. The meshfree sub-domains are discretized into sets of points associated by compact weight functions. For the simplicity of illustration, in the following derivation, we assume there is only one meshfree domain and one FE domain.

3.1. Coupled meshfree/finite element approximation

In the coupled model, the finite element approximation remains in the finite element sub-domains. The meshfree approximation is so constructed in the meshfree sub-domains that the continuity of the approximation remains across the interface between the finite element and meshfree sub-domains or across the interface between any two meshfree sub-domains. The function $\mathbf{u}(\mathbf{X})$ with $\mathbf{X} \in \Omega$ and $\Omega = \Omega_{FEM} \cup \Omega_{meshfree}$ is approximated by

$$\mathbf{u}^h(\mathbf{X}) = \begin{cases} \sum_{L=1}^{KP} \phi_L^{[m]}(\mathbf{X}) \mathbf{d}_L; & \forall \mathbf{X} \in \Omega_{FEM} \\ \sum_{I=1}^{NP} \psi_I^{[n]}(\mathbf{X}; \mathbf{X} - \mathbf{X}_I) \left[\mathbf{d}_I - \sum_{J=1}^{MP} \phi_J^{[m]}(\mathbf{X}_I) \mathbf{d}_J \right] + \sum_{L=1}^{MP} \phi_L^{[m]}(\mathbf{X}) \mathbf{d}_L; & \forall \mathbf{X} \in \Omega_{meshfree} \end{cases} \quad (7)$$

$$= \sum_{I=1}^{NP} \psi_I^{[n]}(\mathbf{X}) \mathbf{d}_I; \quad \forall \mathbf{X} \in \Omega_{meshfree}$$

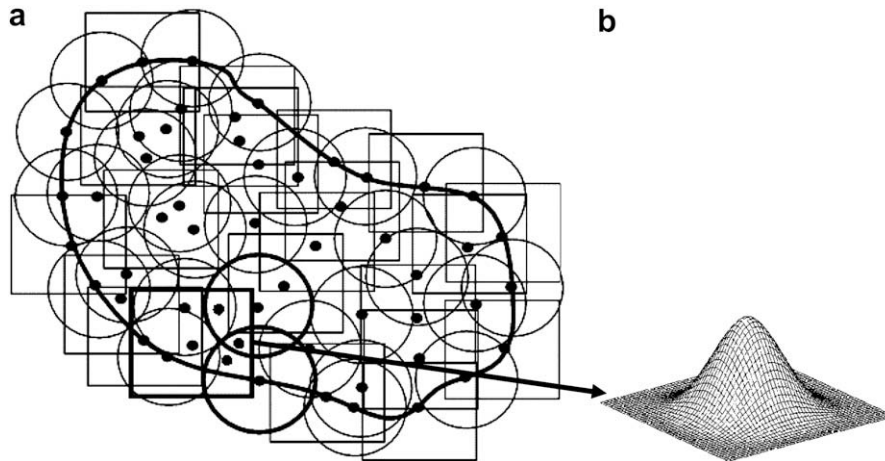


Fig. 2. Example of meshfree discretization and shape function. (a) Meshfree discretization. (b) Meshfree shape function.

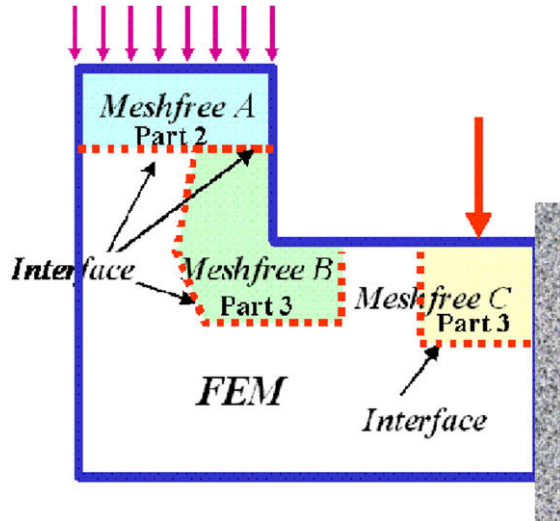


Fig. 3. Example of a coupled meshfree/finite element model.

In Eq. (7), ϕ_L is the regular finite element shape function and KP is the total number of nodes per element. Also, $\Gamma_{\text{Interface}} = \Omega_{\text{FEM}} \cap \Omega_{\text{meshfree}}$, NP is the total number of meshfree points, and MP is the total number of the finite element nodes which are on the interface and whose supports cover point \mathbf{X} . $\psi_i^{[n]}(\mathbf{X})$ is the coupled meshfree/FE shape function. In order to keep the approximation near the interface to be close to the original meshfree approximation, MP in Eq. (7) only involves the nodes along the interface instead of an ‘element’ in the meshfree domain. Therefore, $\psi_i^{[n]}(\mathbf{X})$ will degenerate to the conventional Moving Least Squares approximation if \mathbf{X} is not within the domain of influence from any interface nodes. Later on, this coupling technique is going to be extended to the imposition of essential boundary conditions and contact surfaces to maintain the meshfree nature in the computation. When the finite element interpolation order m is equal to the reproducing order n , it can be proved that

$$\hat{\psi}_I(\mathbf{X}) = 0 \text{ for all nodes } \{I : \text{support}(\psi_I) \cap \Gamma_{\text{Interface}} \neq \emptyset\} \text{ and } \mathbf{X} \in \Gamma_{\text{Interface}} \quad (8)$$

Eq. (8) is called the *interface constraint*, i.e. the MLS shape function of all internal points becomes zero when being evaluated at the interface. If the *interface constraint* is satisfied, the resulting solution approximation of Eq. (7) becomes

$$u_i^h(\mathbf{X}) = \sum_{j=1}^{MP} \phi_j^{[m]}(\mathbf{X}) d_{ij} \quad \forall \mathbf{X} \in \Gamma_{\text{Interface}} \text{ for } i = 1, 2 \text{ and } 3 \quad (9)$$

In other words, the shape functions on the interface are reduced to the standard finite element shape functions and possess the Kronecker delta property. Therefore, there are no conforming problems for the shape functions across the interface.

The proposed method can be considered as one of the ‘compatibility coupling’ methods [18]. Compared to the other existing coupling methods, the proposed method does not require the introduction of ramp functions, Lagrange multipliers, bridging domain, or any special treatment such as the use of visibility criterion in the hybrid approximation. The proposed coupling method avoids the finite-element-like approximation near the interfaces and boundaries in the meshfree domain since the domain influences of interface and boundary nodes are controlled by the support size of interface and boundary nodes as shown in Fig. 4. The extension of this coupling technique to the imposition of essential boundary condition in meshfree domain can also be directly applied. It will be proved later in this paper that the proposed coupling method will satisfy the patch test when two integration constraints are met in the domain integration. Those special properties make the proposed coupling method attractive in the large-scale computation such as the crashworthiness simulation. However, the major disadvantage of this method is the identification of problematic area to be replaced by the meshfree approximation and the requirement of extra pre-processing time to single out the problematic area within a part, which may be troublesome in the full car simulation. For simplicity, it is suggested to replace the whole problematic part from the FEM model by the meshfree formulation. Fortunately, this is very easy to be done in LS-DYNA input card and that requires no pre- and post-processing time.

A one-dimensional example is presented in Fig. 4 to demonstrate how the proposed shape function near the interfaces meets the Kronecker delta property. It is noted that the gradient of the shape function is discontinuous across the interfaces and boundaries, which means in the proposed coupling approach the strain field is discontinuous within an element size from the interfaces and boundaries.

3.2. Coupled meshfree/finite element method for explicit dynamic simulation

Having the coupled meshfree/FE shape functions constructed, we now can use them to solve dynamic problems. A Lagrangian kernel function introduced by Chen et al. [5] for large deformation problems is employed. In this approach, the kernel functions are evaluated using the distance of material particles at the undeformed configuration. Consider a body initially occupying a domain Ω_X and deforming into a configuration with domain Ω_x , where the material behavior is described by tracing the same material point at any time t , $\mathbf{x} = \phi_t(\mathbf{X})$, throughout the history of the deformation.

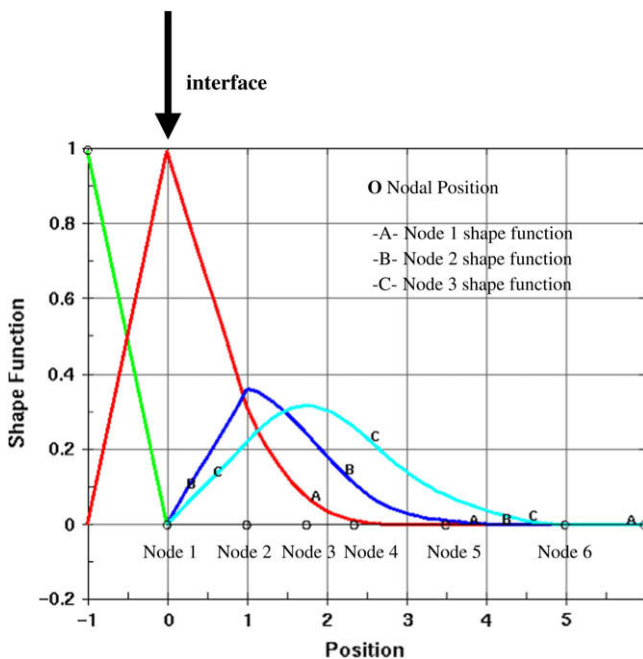


Fig. 4. One dimensional shape functions near the interface for the proposed method.

The motion and deformation of the body is governed by the following equilibrium equations:

$$\rho \ddot{\mathbf{u}} = \nabla \cdot \boldsymbol{\sigma} - \mathbf{f}_b \text{ in } \Omega_{\mathbf{x}}, \Omega_{\mathbf{x}} = \Omega_{FEM} \cup \Omega_{meshfree} \quad (10)$$

with prescribed boundary conditions and given initial conditions:

$$\begin{cases} \mathbf{u} = \mathbf{g} \text{ on } \Gamma_g \\ \boldsymbol{\sigma} \cdot \mathbf{n} = \mathbf{h} \text{ on } \Gamma_h \end{cases} \quad (11)$$

$$\begin{cases} \mathbf{u}(\mathbf{X}, 0) = \mathbf{u}^0(\mathbf{X}) \\ \dot{\mathbf{u}}(\mathbf{X}, 0) = \dot{\mathbf{u}}^0(\mathbf{X}) \end{cases} \quad (12)$$

In Eq. (10), ρ is the mass density and \mathbf{f}_b is the body force. The solution of this set of governing equations can be constructed in the framework of Galerkin weighted residual method with the coupled meshfree/finite element approximation for the unknown variable and the test function. The test function is designed to be $\delta \mathbf{u}(\mathbf{X}) \in Q_0$, $Q_0 = \{\delta \mathbf{u} | \delta \mathbf{u} \in C^0(\mathbf{X}), \delta \mathbf{u} = 0 \text{ on } \Gamma_g\}$, then the corresponding weak form in an updated Lagrangian formulation is

$$\int_{\Omega_{\mathbf{x}}} \rho \delta \mathbf{u} \cdot \ddot{\mathbf{u}} d\Omega = \int_{\Omega_{\mathbf{x}}} \delta \mathbf{u} \cdot \nabla \cdot \boldsymbol{\sigma} d\Omega - \int_{\Omega_{\mathbf{x}}} \delta \mathbf{u} \cdot \mathbf{f}_b d\Omega - \int_{\Gamma_h} \delta \mathbf{u} \cdot \mathbf{h} d\Gamma. \quad (13)$$

The discretization is achieved by applying Eq. (7) in the approximation of $\delta \mathbf{u}$ and \mathbf{u} . In the explicit time integration, the final form of the equations is

$$\delta \mathbf{U}^T \mathbf{M} \ddot{\mathbf{U}} = \delta \mathbf{U}^T \mathbf{R}, \quad (14)$$

where \mathbf{U} is the generalized displacement vector whose values are not the nodal displacements due to the non-Kronecker delta property of the EFG shape functions. Similarly, \mathbf{M} is generalized mass matrix and \mathbf{R} is the generalized residual force vector. Their definitions are

$$\begin{cases} \mathbf{U} = [\mathbf{d}_1^T & \mathbf{d}_2^T & \dots & \mathbf{d}_{IP}^T]^T \\ \mathbf{d}_I = [d_{1I} & d_{2I} & d_{3I}]^T \\ \mathbf{M}_{IJ} = \int_{\Omega_{\mathbf{x}}} \rho \hat{\psi}_I(\mathbf{x}) \hat{\psi}_J(\mathbf{x}) d\Omega = \int_{\Omega_{\mathbf{x}}} \rho^0 \hat{\psi}_I(\mathbf{X}) \hat{\psi}_J(\mathbf{X}) d\Omega \\ \mathbf{R}_I = \int_{\Omega_{\mathbf{x}}} \mathbf{B}_I^T(\mathbf{x}) \boldsymbol{\sigma} d\Omega - [\hat{\psi}_I(\mathbf{x}) \mathbf{h}]|_{\Gamma_h} - \int_{\Omega_{\mathbf{x}}} \hat{\psi}_I(\mathbf{x}) \mathbf{f}_b d\Omega \end{cases} \quad (15)$$

$\mathbf{B}_I^T(\mathbf{x})$ is the standard gradient matrix and IP is the total number of discrete points and nodes in the domain. To introduce the meshfree Lagrangian shape function into the approximation of an updated Lagrangian formulation, the strain increment is obtained using the chain rule as $\Delta u_{ij} = \Delta F_{ik} F_{kj}^{-1}$ and is used in the formation of gradient matrix. The stable critical time step follows the Courant–Friedrichs–Lewy stability condition [22]. The nodal displacement vector $\hat{\mathbf{U}}$ is related to the generalized displacement vector \mathbf{U} by

$$\hat{\mathbf{U}} = \mathbf{A} \mathbf{U} \text{ and } A_{IJ} = \hat{\psi}_J(\mathbf{X}_I) \quad (16)$$

and for the mass matrix and residual force we have

$$\hat{\mathbf{M}} = \mathbf{A}^{-T} \mathbf{M} \mathbf{A}^{-1}; \quad (17)$$

$$\hat{\mathbf{R}} = \mathbf{A}^{-T} \mathbf{R} \quad (18)$$

3.2.1. Meshfree domain integration

The numerical integration in Eq. (15) is evaluated by the modified Stabilized Conforming Nodal Integration method (SCNI) in the meshfree domain. The original Stabilized Conforming Nodal Integration method [15] has been developed to meet the integration constraint:

$$\int_{\Omega_{\mathbf{x}}} \mathbf{B}_I^T d\Omega = 0 \text{ for all interior nodes } \{I : \mathbf{X}_I \notin \Gamma_g\} \quad (19)$$

or in its discrete form,

$$\sum_{j=1}^{NP} \nabla \hat{\psi}_I(\mathbf{X}_j) W_j = 0 \text{ for all interior nodes } \{I : \mathbf{X}_I \notin \Gamma_g\} \quad (20)$$

where W_j is the weight of the domain integration point which is evaluated at the node and can be obtained from the Voronoi diagram in the SCNI method [15].

This constraint can be derived with the consideration of a Dirichlet boundary value problem with a linear displacement field. When the shape functions have the Kronecker delta property, the internal force which should be zero at an interior node is calculated by $\int_{\Omega_{\mathbf{x}}} \mathbf{B}_I^T \boldsymbol{\sigma} d\Omega$. Since the stress $\boldsymbol{\sigma}$ is constant for a linear displacement field, consequently $\int_{\Omega_{\mathbf{x}}} \mathbf{B}_I^T d\Omega$ has to be zero to have the exact solution of the Dirichlet boundary value problem. Here we call this the *first integration constraint* considering there is another constraint to be followed next. The derivative of shape function $\nabla_i \hat{\psi}_I(\mathbf{X}_j)$ in Eq. (20) is computed by applying the strain smoothing method and the divergence theorem to yield

$$\nabla_i \hat{\psi}_I(\mathbf{X}_j) = \frac{1}{A_j} \int_{\Gamma_j} \hat{\psi}_I(\mathbf{X}) n_i(\mathbf{X}) d\Gamma \quad (21)$$

where Γ_j is the boundary of the representative domain of point J and A_j is the associated representative area.

In general the coupled shape functions defined in Eq. (7) do not have Kronecker Delta property in the meshfree domain. The internal force is calculated by $(\mathbf{A}^{-T})_{IJ} \int_{\Omega_{\mathbf{x}}} \mathbf{B}_J^T \boldsymbol{\sigma} d\Omega$ in the meshfree formulation. Using the first integration constraint in Eq. (19), we have

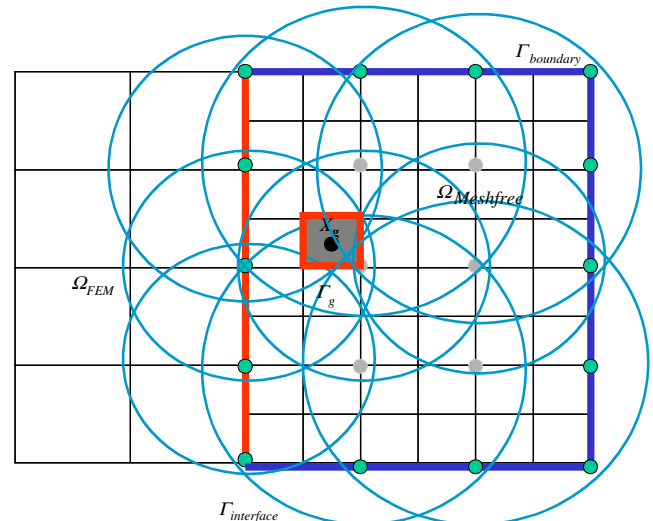


Fig. 5. Strain smoothing of X_g by modified local boundary integration along Γ_g .

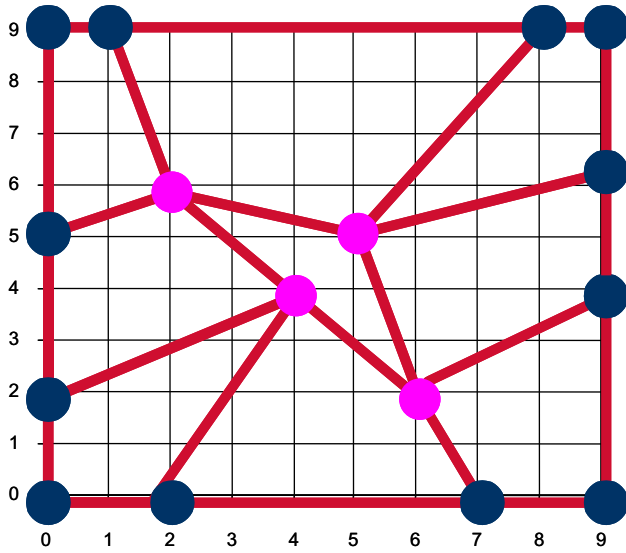


Fig. 6. The discrete model for the patch test.

$$\hat{\mathbf{F}}_I^{\text{int}} = (\mathbf{A}^{-T})_{IJ} \int_{\Omega_x} \mathbf{B}_J^T \boldsymbol{\sigma} d\Omega = (\mathbf{A}^{-T})_{IJ} \int_{\Omega_x} \mathbf{B}_J^T \boldsymbol{\sigma} d\Omega \quad (22)$$

for $\{I: \mathbf{X}_I \notin \Gamma_g\}$ and $\{J: \mathbf{X}_J \in \Gamma_g\}$

To have $\hat{\mathbf{F}}_I^{\text{int}}$ in Eq. (22) to be zero at node I for $\{I: \mathbf{X}_I \notin \Gamma_g\}$, it requires

$$(\mathbf{A}^{-T})_{IJ} \int_{\Omega_x} \mathbf{B}_J^T \boldsymbol{\sigma} d\Omega = 0 \text{ for } \{I: \mathbf{X}_I \notin \Gamma_g\} \text{ and } \{J: \mathbf{X}_J \in \Gamma_g\} \quad (23)$$

We call Eq. (23) the *second integration constraint*. One way to satisfy this constraint is to apply finite element shape functions only along the essential boundaries instead of the background elements:

$$\hat{\psi}_I(\mathbf{X}_J) = \delta_{IJ} \text{ for } \{I: \mathbf{X}_I \in \Gamma_g\}. \quad (24)$$

By doing so the two-dimensional finite element shape functions are incorporated with the three-dimensional meshfree shape functions along the essential boundaries and contact surfaces. In this way, $(\mathbf{A}^{-T})_{IJ}$ in Eq. (23) becomes zero and hence $\hat{\mathbf{F}}_I^{\text{int}}$ becomes zero. The same idea can also be applied to the coupling of FEM and meshfree along the interfaces. Another benefit is that with $\hat{\psi}_I(\mathbf{X}_J) = \delta_{IJ}$ for all essential boundary nodes $\{J: \mathbf{X}_J \in \Gamma_g\}$ the transformation matrix is not needed for the essential boundary treatment anymore. Combining Eq. (24) and Eq. (7), we have the modified coupled meshfree/finite element shape function $\hat{\psi}_I$ as

$$\mathbf{u}^h(\mathbf{X}) = \begin{cases} \sum_{L=1}^{KP} \Phi_L^{[m]}(\mathbf{X}) \mathbf{d}_L; & \mathbf{X}_L \in \Omega_{\text{FEM}} \\ \sum_{I=1}^{NP} \psi_I^{[n]}(\mathbf{X}; \mathbf{X} - \mathbf{X}_I) \left[\mathbf{d}_I - \sum_{J=1}^{MP} \Phi_J^{[m]}(\mathbf{X}_I) \mathbf{d}_J \right] + \sum_{L=1}^{MP} \Phi_L^{[m]}(\mathbf{X}) \mathbf{d}_L & \mathbf{X}_I \in \Omega_{\text{meshfree}} \\ & \mathbf{X}_I \in \Gamma_{\text{Interface}} \text{ or } \mathbf{X}_I \in \Gamma_g \setminus \Gamma_g \end{cases}$$

$$= \sum_{I=1}^{NP} \hat{\psi}_I^{[n]}(\mathbf{X}) \mathbf{d}_I; \quad \mathbf{X}_I \in \Omega_{\text{meshfree}}$$

Table 1

Comparison of solutions of the patch test by the conventional meshfree method using 4 by 4 Gauss integration rule and by the proposed methods.

Exact solution [u_1 u_2]		4 by 4 Gauss integration		Proposed method without the second integration constraint		Proposed method with the second integration constraints	
4.00	4.00	4.09	3.97	4.00	4.00	4.00	4.00
		+2%	−1%	0.0%	0.0%	0.0%	0.0%
6.00	2.00	5.77	3.50	6.00	2.01	6.00	2.00
		−4%	+75%	+1%	+1%	0.0%	0.0%
2.00	6.00	3.26	5.22	2.00	6.00	2.00	6.00
		+63%	−13%	−8%	0.0%	0.0%	0.0%
5.00	5.00	4.84	4.14	5.00	5.00	5.00	5.00
		−3%	−17%	−1%	0.0%	0.0%	0.0%

The first and second integration constraints together ensure the coupled meshfree/FE formulation to pass a linear exactness test of the Dirichlet boundary value problem.

The modified SCNI is equivalent to the two point Gauss integration with local boundary integration performed on each Gauss point. It eliminates hourglass modes which are observed when the original SCNI method is used. It also avoids the use of stabilization force required in the nodal integration method [19]. The background connectivity taken directly from the original meshed model is used. The strain smoothing stabilization originally proposed in [15] is modified in this research as

$$\bar{\nabla} u_i^h(\mathbf{X}_g) = \frac{1}{W_g} \int_{\Gamma_g} \mathbf{n} \cdot \mathbf{u}_i^h d\Gamma \quad (26)$$

where Γ_g is the boundary of the representative domain corresponding to the integration point \mathbf{X}_g ; $\bar{\nabla}$ is the smoothed or modified gradient operator; and \mathbf{n} is the normal to the boundary line Γ_g . The smoothed or modified strain computed from Eq. (26) is in a sense ‘averaged’ and assigned to the point \mathbf{X}_g . The representative strain smoothing stabilization using the modified local boundary integration is shown in Fig. 5, where the supports with solid lines denote the supports of meshfree discrete points contributing to the strain smoothing at \mathbf{X}_g . This smoothed strain obtained from the proposed local boundary integration scheme satisfies the first integration constraint

$$\int_{\Omega} \bar{\mathbf{B}}_I^T d\Omega = 0 \text{ for all interior nodes} \quad (27)$$

where $\bar{\mathbf{B}}_I$ is the modified gradient matrix with components computed from Eq. (26).

$$\forall \mathbf{X} \in \Omega_{\text{FEM}}$$

$$\mathbf{u}^h(\mathbf{X}) = \begin{cases} \sum_{L=1}^{MP} \Phi_L^{[m]}(\mathbf{X}) \mathbf{d}_L & \mathbf{X}_L \in \Gamma_{\text{Interface}} \text{ or } \mathbf{X}_L \in \Gamma_g \\ \sum_{L=1}^{MP} \Phi_L^{[m]}(\mathbf{X}) \mathbf{d}_L & \mathbf{X}_L \in \Omega_{\text{meshfree}} \end{cases} \quad (25)$$

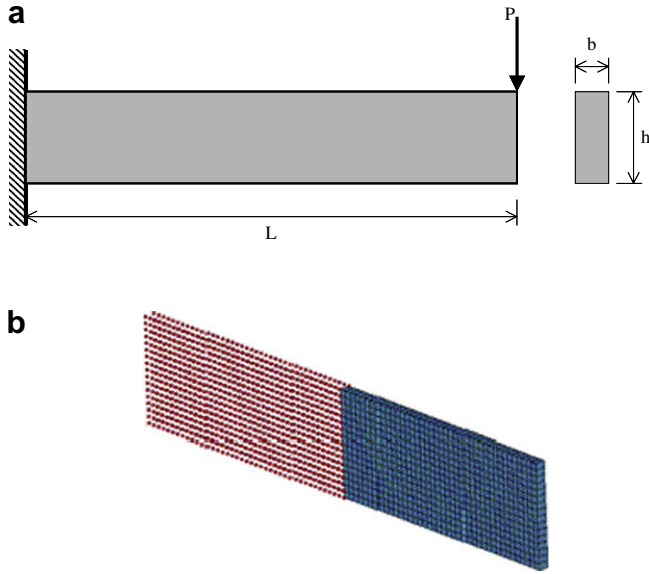


Fig. 7. (a) Problem description of a 3D cantilever beam. (b) Discretization of the cantilever beam with the coupled meshfree/FE method.

To introduce the strain smoothing formulation of Eq. (27) into the Galerkin approximation, a mixed variation principle based on an assumed strain method is considered [15, 16], which is

$$\int_{\Omega_x} \rho \delta \mathbf{u} \cdot \ddot{\mathbf{u}} d\Omega = \int_{\Omega_x} \delta \bar{\boldsymbol{\varepsilon}} : \boldsymbol{\sigma} d\Omega - \int_{\Omega_x} \delta \mathbf{u} \cdot \mathbf{f}_b d\Omega - \int_{\Gamma_h} \delta \mathbf{u} \cdot \mathbf{h} d\Gamma \quad (28)$$

where \$\bar{\boldsymbol{\varepsilon}}\$ is the assumed strain computed from Eq. (26).

For explicit time integration, a row-sum method is used for the construction of the lumped mass. Recall the consistent mass matrix in Eq. (15), and perform the row-sum method. The diagonalized mass vector is obtained as

$$\mathbf{M}_I^{lump} = \sum_{j=1}^{IP} M_{Ij} = \int_{\Omega_x} \rho^0 \hat{\psi}_I(\mathbf{X}) \sum_{j=1} \hat{\psi}_j(\mathbf{X}) d\Omega = \int_{\Omega_x} \rho^0 \hat{\psi}_I(\mathbf{X}) d\Omega \quad (29)$$

Compared to the conventional meshfree method using Moving Least Squares approximation, the proposed method yields the same

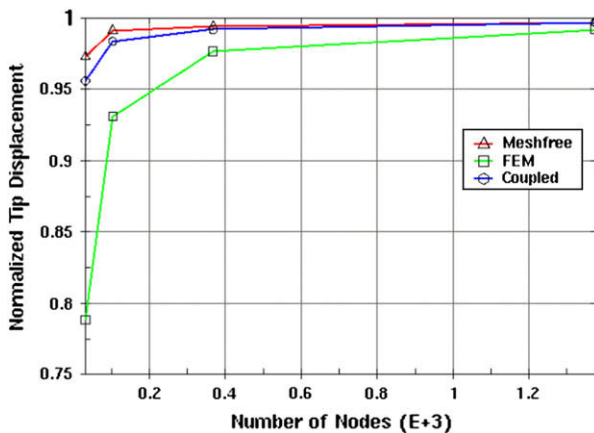


Fig. 8. Comparisons of the h-convergence of the tip deflection solution with three different methods.

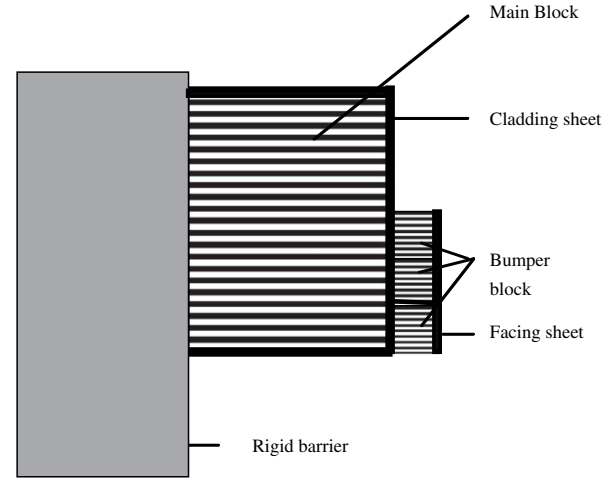


Fig. 9. The description of an offset deformable barrier.

nodal lumped mass when the support of the node does not cover the interface or boundary. When the nodal support covers any interface or boundary, the resultant nodal lumped mass will be different from the one obtained from the conventional meshfree method using Moving Least Squares approximation. Since the coupled meshfree and finite element shape functions satisfy at least the first-order reproducing condition, the total sum of nodal lumped mass will still satisfy the conservation of mass.

The resulting discrete matrix is given by

$$\mathbf{M}^{lump} \ddot{\mathbf{U}} = \mathbf{f}^{ext} - \mathbf{f}^{int}(\hat{\nabla} u_i^h) \quad (30)$$

where

$$\mathbf{M}_I^{lump} = \int_{\Omega_x} \rho^0 \hat{\psi}_I(\mathbf{X}) d\Omega \quad (31)$$

$$\mathbf{f}_I^{int} = \int_{\Omega_x} \bar{\mathbf{B}}_I^T \cdot \bar{\boldsymbol{\sigma}}(\bar{\mathbf{F}}) d\Omega \quad (32)$$

$$\mathbf{f}_I^{ext} = -[\hat{\psi}_I(\mathbf{x}) \mathbf{h}]|_{\Gamma_h} - \int_{\Omega_x} \hat{\psi}_I(\mathbf{x}) \mathbf{f}_b d\Omega \quad (33)$$

where \$\bar{\mathbf{F}}\$ is the smoothed deformation gradient.

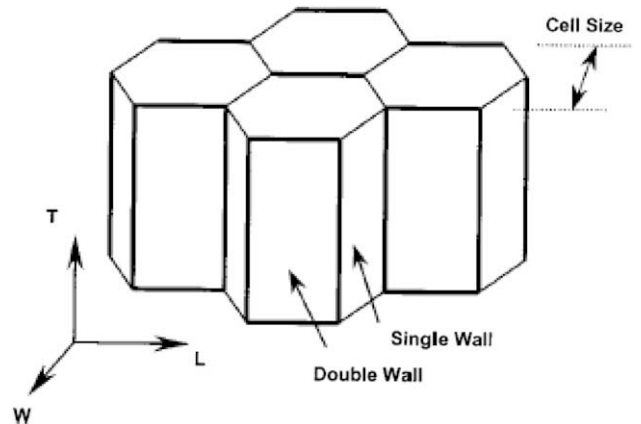


Fig. 10. Honeycomb structure and principal directions (after Zhou and Mayer [24]).

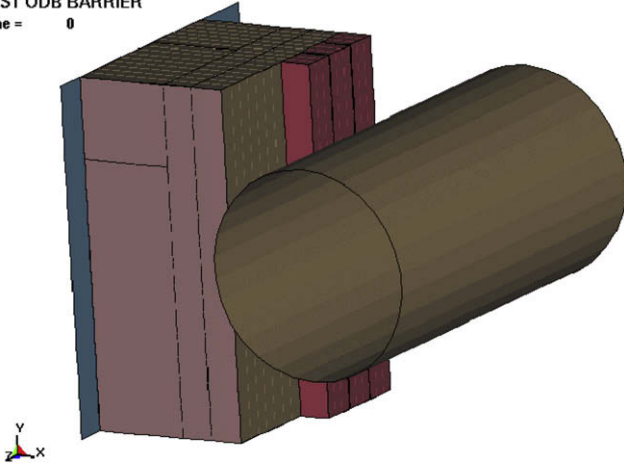
FAST ODB BARRIER
Time = 0

Fig. 11. Problem description of the ODB test.

The numerical integration for $\mathbf{f}_l^{\text{int}}$ by the proposed local boundary integration scheme is

$$\mathbf{f}_l^{\text{int}} = \sum_{IE=1}^{NE} \sum_{g=1}^{nint} \mathbf{B}_l^T(\mathbf{X}_g) \bar{\mathbf{G}}^T \cdot \bar{\boldsymbol{\sigma}}(\bar{\mathbf{F}}(\mathbf{X}_g)) \bar{\mathbf{J}}(\mathbf{X}_g) A_g \quad (34)$$

where NE is the total number of elements within each sub-domain g of $nint$ in background mesh IE under the influence of node l . $nint$ is the number of the sub-domain per each background mesh. $\bar{\mathbf{G}}^T$ is the transform matrix of the inverse of the smoothed deformation gradient from Eq. (27) for the usage of the Lagrangian kernel function. For example, in two-dimensions,

$$\bar{\mathbf{G}}^T = \begin{bmatrix} \bar{F}_{11}^{-1} & 0 & \bar{F}_{21}^{-1} & 0 \\ 0 & \bar{F}_{22}^{-1} & 0 & \bar{F}_{12}^{-1} \\ \bar{F}_{12}^{-1} & \bar{F}_{21}^{-1} & \bar{F}_{22}^{-1} & \bar{F}_{11}^{-1} \end{bmatrix} \quad (35)$$

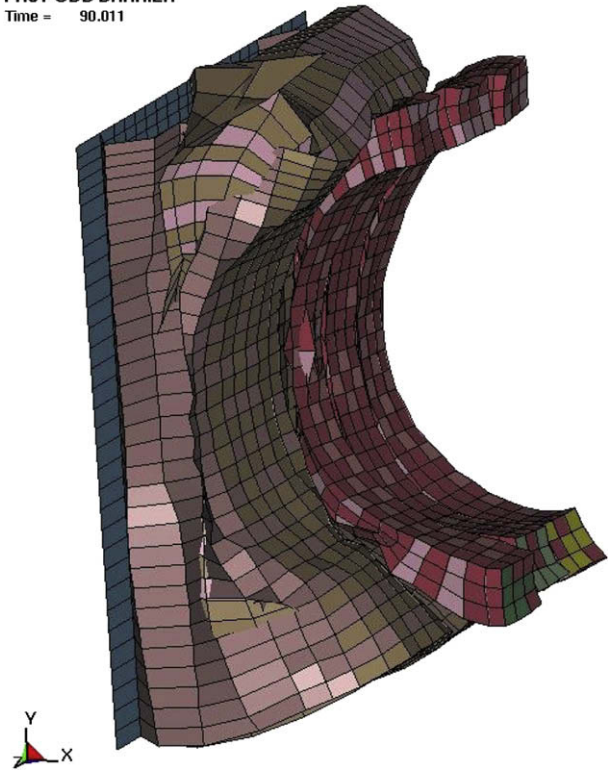
FAST ODB BARRIER
Time = 90.011

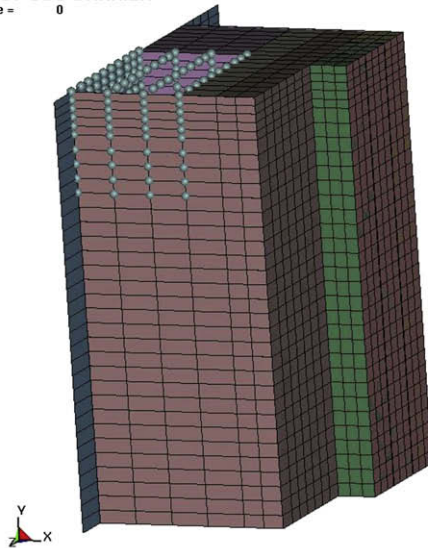
Fig. 12. The ODB deformation from the conventional FE analysis.

4. Numerical examples

We have implemented the coupled meshfree/FE method into LS-DYNA version 971 and its later versions for industrial applications. It is recommended that engineers should consider the meshfree formulation for the parts which experience large deformation and whose finite element formulations lead to negative element volumes.

FAST ODB BARRIER
Time = 0

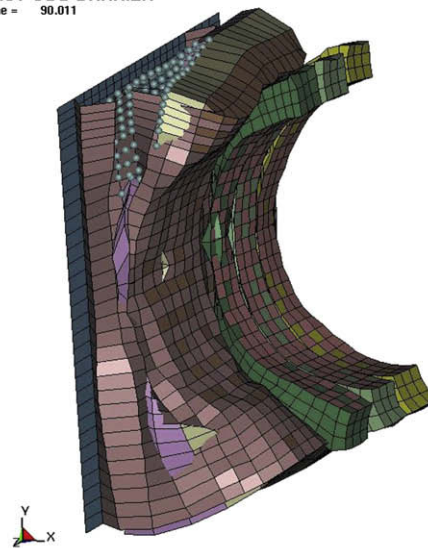
a



The Coupled Model

FAST ODB BARRIER
Time = 90.011

b



The Deformation

Fig. 13. The coupled meshfree/finite element ODB model and resulting deformation.

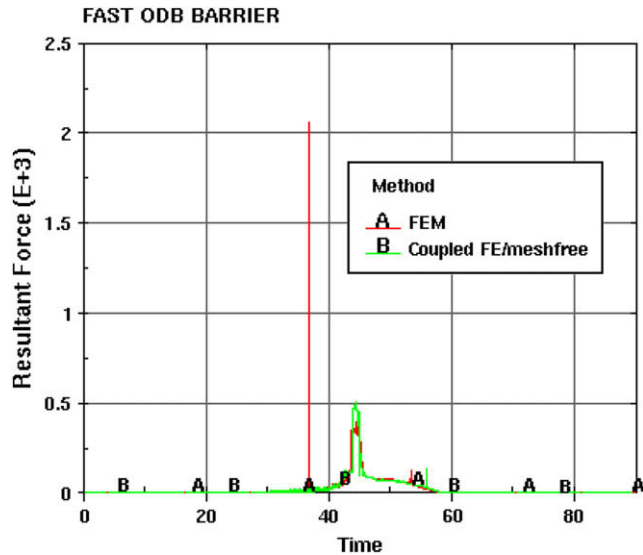


Fig. 14. The response force histories in the ODB test (units: ms for time, MPa for force).

In this section, we will present the applications of the coupled meshfree/FE method in automotive problems. Before we present any practical applications, we will evaluate its performance in a simple patch test and do a convergence study using a cantilever beam problem.

4.1. Patch test

To evaluate the numerical performance by this new solution approximation and integration scheme, the following Laplace

equation with Dirichlet boundary conditions is solved. The problem statement is

$$\nabla^2 u(\mathbf{x}) = 0, \text{ in } \Omega = (0, 9) \times (0, 9) \quad (36)$$

$$\mathbf{u}(\mathbf{x}_u) = \mathbf{x}_u, \text{ on } \Gamma_u \quad (37)$$

Fig. 6 shows the discrete model, which will be analyzed using the meshfree method. A cubic spline function is employed as the weight function. A support size of 7.2 is used in this study. This value is chosen to cover enough points for the construction of shape functions. Linear basis functions are used to construct the shape functions. The exact solution for this problem is $\mathbf{u}(\mathbf{x}_I) = \mathbf{x}_I$ for $\mathbf{x}_I \in \Omega \setminus \Gamma_u$. Table 1 gives the comparison of results and corresponding errors using 4 by 4 Gauss quadrature rule and the proposed method with or without the second integration constraints. Table 1 shows that only the proposed method with the second integration constraints imposed gives the exact solutions for this problem. That means it passes the linear patch test and can exactly reproduce a linear field. It is also noted that any support size greater than 7.2 will not affect the result in the patch test using the proposed method when the second integration constraint is imposed.

4.2. Cantilever beam

In this example, a three-dimensional cantilever beam as shown in Fig. 7a is analyzed to study the convergence and accuracy of the proposed coupling method. The beam is fixed at one end and is subjected to a parabolic traction at the other end. Since the beam is relatively thin, a plane stress condition can be considered to yield the analytical solution [23]. The following parameters are used for

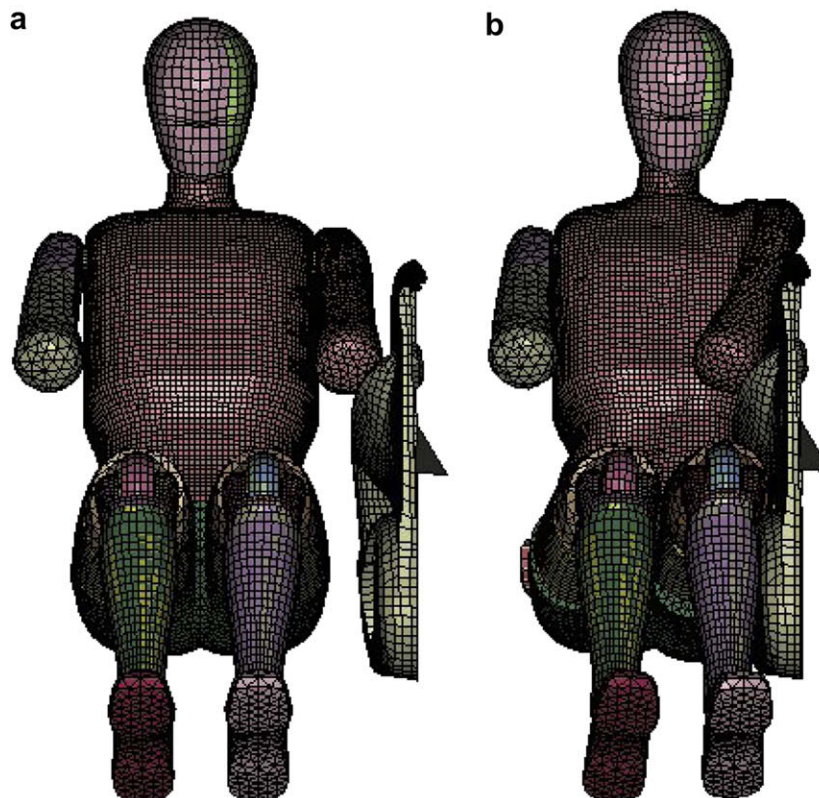


Fig. 15. The finite element dummy side impact model. (a) The finite element model. (b) The deformation at $t = 20$ ms.

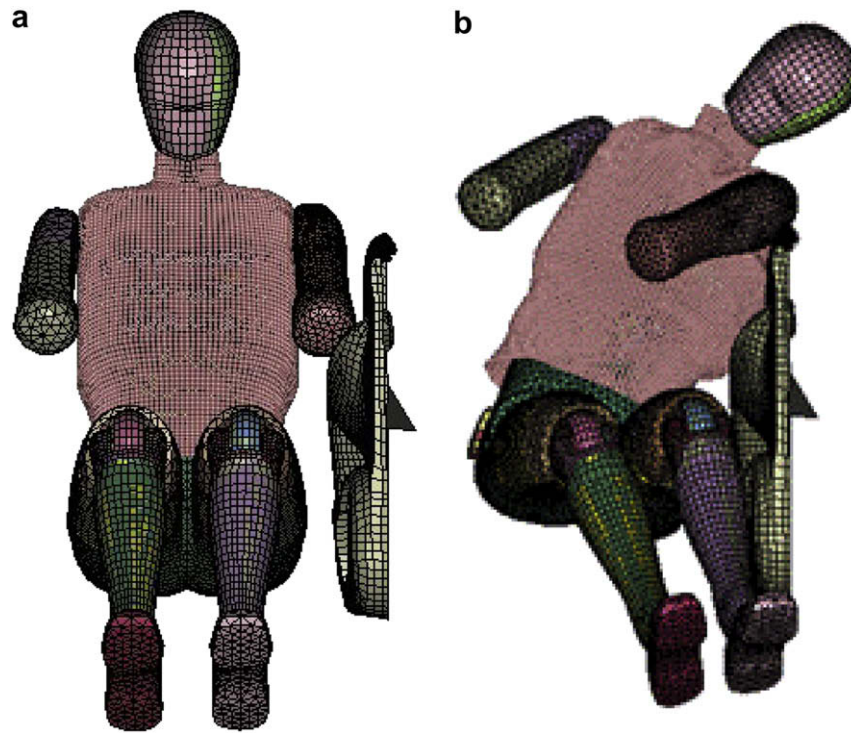


Fig. 16. The coupled meshfree/FE side impact dummy model (a) The coupled meshfree/FE model. (b) The deformation at $t = 60$ ms.

this problem: Young's modulus $E = 1.0$ GPa; Poisson's ratio $\nu = 0.3$; $L = 50$ mm; $h = 10$ mm; $b = 1$ mm. To model it using the coupled meshfree/FE method, the beam is divided into two parts. The part near the free end is modeled by the fully integrated FEM and the other part is modeled by the meshfree method as shown in Fig. 7b. Regular discretizations with $3 \times 3 \times 3$ Gaussian quadrature were used for two parts. Normalized support size being 1.5 was used for the meshfree shape function computation.

The problem is also modeled by the FEM and the meshfree method in order to compare the solutions of the three methods: the FEM, the meshfree method and the coupled meshfree/FE method. Fig. 8 shows the normalized tip displacement for different

refinements obtained from the three methods. The results show that the solutions from the three methods converge to the analytical one as the models are refined. The meshfree method gives the most accurate solution for the same discretization compared to the other two methods. The performance of the proposed coupled meshfree/FE method is between the FEM and the meshfree method as expected. Since in the coupled model the meshfree method is used in the part near the fixed end which exhibits most deformation, the result from the coupled meshfree/FE analysis is close to the one obtained from the meshfree method.

4.3. Frontal Offset Deformable Barrier

A frontal Offset Deformable Barrier (ODB) is used in the Insurance Institute for Highway Safety (IIHS) 40MPH Frontal Offset Crash Test, European New Car Assessment Program (Euro NCAP)—64KPH (40MPH) Frontal Offset Crash Test, and European Type Approval Test—56KPH (35MPH) Frontal Offset Crash Test. As shown in Fig. 9, the barrier is comprised of two elements: a fixed rigid barrier and a deformable face. The deformable face consists of two aluminum honeycomb blocks with aluminum covering. The honeycomb blocks consist of many thin aluminum hexagonal cells which have double thickness walls with adhesive in between. Fig. 10 illustrates the structure of the honeycomb cell. The direction parallel to the hexagonal cell prisms is referred as the axial direction. The main block has a height of 650 mm, a width of 1000 mm and a depth of 450 mm (in the direction of honeycomb cell axis), and has crush strength of 0.342 MPa [24] and nominal density of 28.6 kg/m^3 . It is covered with aluminum cladding sheet at the top, bottom and rear faces of block. The bumper element honeycomb has a height of 330 mm, a width of 1000 mm and a depth of 90 mm and has crush strength of 1.711 MPa and nominal density of 82.6 kg/m^3 . Its rear face is covered with an aluminum facing sheet. The parts are bonded together by polyurethane adhesives.

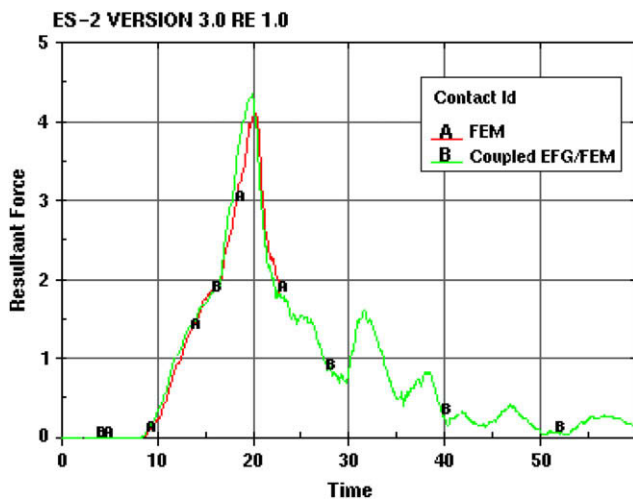


Fig. 17. The response curve comparison in the dummy component test (units: ms for time, MPa for force).

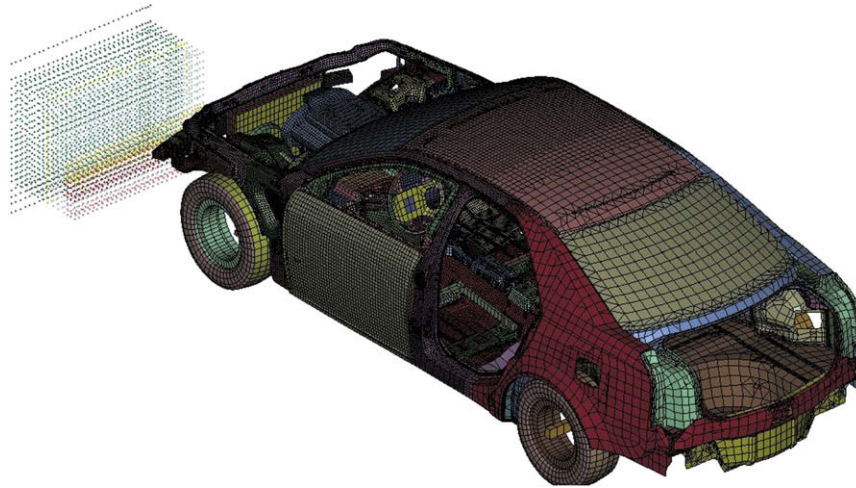


Fig. 18. The coupled meshfree/FE model of the IIHS frontal ODB impact problem.

In the discrete model, the rigid barrier is treated as a constrained rigid body. The deformable face blocks are modeled by solid elements with LS-DYNA material type 126, *MAT_MODIFIED_HONEYCOMB, and cladding and facing sheets are modeled by shell elements with LS-DYNA material type 3, *MAT_PLASTIC_KINEMATIC. The detailed material properties of the honeycomb blocks can be found in Zhou's work [24]. For the aluminum sheet, the mass density is $2.68 \times 10^{-3} \text{ kg/m}^3$ with Young's modulus being 70.0 GPa, Poisson ratio being 0.33, yield stress being 180 MPa and tangent modulus being 550 MPa. In this testing, the barrier is impacted by a rigid cylinder that is moving toward the barrier along

axial direction with initial velocity being 15 mm/ms, as shown in Fig. 11. The FE analysis of this problem shows unrealistic deformation when the cylinder pushes deepest into the barrier, shown in Fig. 12, where some elements in the left upper corner of the block exhibit excessive distortion.

To test the effectiveness of coupled meshfree/FE approach, the brick elements in the left upper corner of the block switch to the meshfree formulation, while the others remain their original FE formulations, shown in Fig. 13a. The ratio of the meshfree Degrees Of Freedom (DOFs) over the total DOFs in the model is 0.076:1.0. Fig. 13b gives the deformation from the coupled meshfree/FE

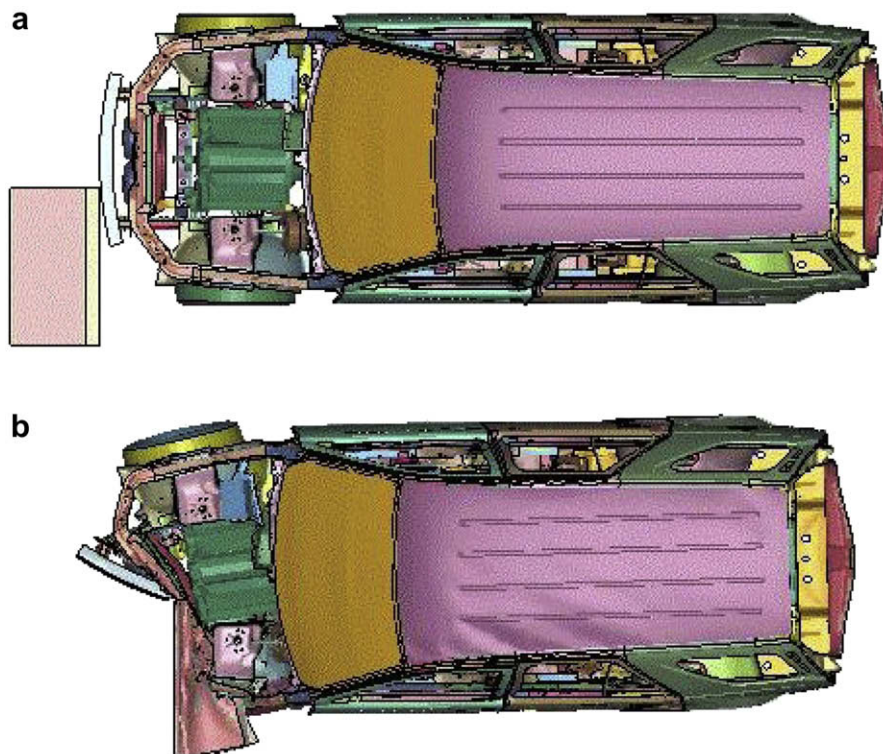


Fig. 19. Deformations from the coupled meshfree/FE analysis of the IIHS frontal ODB impact problem (a) Undeformed configuration at $t = 0 \text{ ms}$. (b) Deformed configuration at $t = 80 \text{ ms}$.

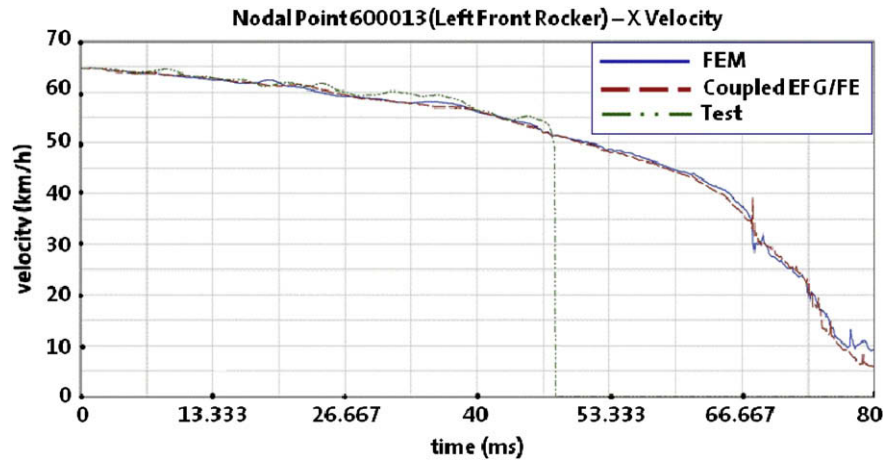


Fig. 20. The velocity histories of the left front rocker in the IIHS frontal ODB impact problem.

analysis. No excessive distortion at the upper corner of the block is observed. Fig. 14 gives the comparison of response force histories on the cylinder. The force curve from the FE analysis shows a sudden noise at the time when the elements at the upper corner of the block started to experience excessive deformation. The numerical noise often leads to numerical instabilities and hence fails analyses. In the coupled analysis, this discontinuity does not exist. The ratio of the CPU time consumed by the coupled analysis over one by the FE analysis is 1.12:1 in this test, where the coupled analysis consumed 12% higher CPU than the finite element analysis.

4.4. European side impact dummy component test simulation

A European side impact dummy component test is simulated. As shown in Fig. 15, the dummy is impacted from the left side by a door panel. The original finite element model of the problem is shown in Fig. 15a. The FE analysis showed excessive element deformation in the upper rib foam of the dummy when the door panel pushed onto the dummy, see Fig. 15b. Negative element volume occurred, led to numerical instabilities and hence failed analyses right after $t = 20$ ms. In the coupled meshfree/FE model, all three rib foams are modeled by the meshfree solid formulation. The coupled meshfree/FE analysis with this modification failed again due to the element distortion in the dummy jacket. Further on, the dummy jacket is modeled by the meshfree shell formulation. The coupled meshfree/FE analysis is then successfully completed. Fig. 16a shows the coupled meshfree/FE model and Fig. 16b shows its final deformation. In the model, the ratio of the meshfree DOFs over the total DOFs in the model is 0.189:1.0.

Fig. 17 gives the comparison of the response force histories. The force curve from the FE analysis climbs up quickly at the time when the dummy starts to experience excessive deformation, which often contributes to the numerical instabilities. In the FE analysis, negative element volume occurs after this peak and the analysis stops due to the numerical instability. In the coupled analysis, no element distortion occurs and the analysis is completed. The response curves from both analyses agree with each other very well

before the distortion occurs. The CPU consumed by the FE analysis up to $t = 20$ ms is 9083 s. For the coupled analysis, the simulation runs up to $t = 60$ ms, and 50194 s is consumed. The normalized CPU ratio between the FE analysis and the coupled analysis is about 1.0:2.0 in this testing.

4.5. Insurance Institute for Highway Safety frontal offset deformable barrier impact

Insurance Institute for Highway Safety (IIHS) frontal offset deformable barrier impact test is simulated. As shown in Fig. 18, the ODB model is impacted by a vehicle at 40 MPH. For this problem the original finite element analysis can run successfully. Here we use the problem to see the robustness of this coupled meshfree/FE method in simulating a full vehicle crash test. In the coupled analysis, as shown in Fig. 16 the entire barrier is modeled by the meshfree formulation with all the null shells removed. The null shells are used in the original FE barrier model to wrap each solid element so as to prevent negative element volume problems. They are unnecessary in the meshfree model. The ratio of the meshfree DOFs over the total DOFs in the model is 0.015:1.0. The coupled meshfree/FE analysis is successfully completed. Fig. 19 shows the final deformation, where the barrier is severely crushed. Fig. 20 plots the velocity histories of the left front rocker from the original FE analysis, the coupled meshfree/FE analysis and the physical test. It shows that the velocity curve calculated from the coupled analysis agrees very well with the test data. Table 2 gives the CPU time comparison between the original FE simulations and the coupled meshfree/FE simulations when various numbers of CPU are used. The coupled method consumes slightly higher CPU time than the original FEM.

5. Conclusions

This paper presents a newly developed coupled meshfree/finite element analysis tool in LS-DYNA for the analysis of crash and safety problems. The Element-Free Galerkin method was employed in the meshfree formulation. An interface constraint was developed to ensure the continuity of the approximation across the interfaces between the meshfree and FE zones and between the meshfree and meshfree zones. To satisfy linear exactness in the meshfree Galerkin approximation of the Dirichlet boundary value problems, two integration constraints have been developed. A local boundary integration scheme with the coupled meshfree/FE shape function

Table 2

Normalized CPU time comparison between the normal FE analysis and the coupled meshfree/FE analysis.

Number of CPU's	1	2	4	8
FEM	1.00	0.70	0.39	0.25
Coupled Meshfree/FEM	1.11	0.77	0.44	0.27

has been developed to satisfy the two integration constraints, so as to eliminate the possible hourglass mode and to reduce the computation time on the imposition of essential boundary conditions. A new lumping method for the mass matrix and body force has been developed for the explicit dynamic computation. The coupled meshfree/finite element method can pass the linear patch test exactly. The convergence study shows that the solution from the coupled method converges to the analytical one as the model is refined. The rate of h-convergence of the coupled analysis is larger than the FE analysis but smaller than the meshfree method.

Three problems that often encounter element distortion difficulties were employed to study the performance of the coupled method in dealing with large deformation. They are an offset deformable barrier component test, a European side impact dummy component test and an IIHS ODB impact test. All three testing problems have showed that the coupled meshfree/finite element models were numerically more stable in dealing with large deformation than the finite element models. The increase in required computer resource was limited when only the problematic area was modeled by the meshfree formulation. The problematic area usually is identified by the severe mesh distortion observed from the finite element result. It is also worthwhile to spend this extra time to gain the big savings in running multiple analyses in a trial-and-error fashion to find a numerically stable solution. From the study we can conclude that the coupled meshfree/FE method provides a robust tool for simulating problems involving excessive material distortion. It is especially true for the crashworthiness analyses which by nature deal with severe crushing problems.

Acknowledgments

The authors wish to thank Majeed Bhatti, Yih-Charng Deng, Henry Schuyten, Ye-Chen Pan, Yi-Pen Cheng, Richard Lyscas, Joseph Wu, Jerry Pan and Sharon Xiao of General Motors for their valuable discussions on the meshfree applications.

References

- [1] Mayer R, Webb S, Wang JT, Liu B, Zhou Q. Sled tests and simulations of offset deformable barrier. *International Journal of Vehicle Safety* 2005;1:238–51.
- [2] Randles PW, Libersky LD. Smoothed particle hydrodynamics: some recent improvements and applications. *Computational Methods in Applied Mechanical Engineering* 1996;139:375–408.
- [3] Belytschko T, Lu YY, Gu L. Element free Galerkin method. *International Journal of Numerical Methods in Engineering* 1994;37:229–56.
- [4] Liu WK, Jun S, Zhang YF. Reproducing kernel particle methods. *International Journal of Numerical Methods in Fluids* 1995;20:1081–106.
- [5] Chen JS, Pan C, Wu CT, Liu WK. Reproducing kernel particle methods for large deformation analysis of nonlinear structures. *Computational Methods in Applied Mechanical Engineering* 1996;139:195–227.
- [6] Melenk JM, Babuska I. The partition of unity finite element method: basic theory and applications. *Computational Methods in Applied Mechanical Engineering* 1996;139:289–314.
- [7] Duarte CAM, Oden JT. A H-P adaptive method using clouds. *Computational Methods in Applied Mechanical Engineering* 1996;139:237–62.
- [8] Krongauz Y, Belytschko T. EFG approximation with discontinuous derivatives. *International Journal for Numerical Methods in Engineering* 1998;41:1215–33.
- [9] Fleming M, Chu YA, Moran B, Belytschko T. Enriched element-free Galerkin methods for crack tip fields. *International Journal for Numerical Methods in Engineering* 1997;40(8):1483–504.
- [10] Belytschko T, Organ D, Krongauz Y. A coupled finite element–element-free galerkin method. *Computational Mechanics* 2000;51:221–58.
- [11] Huerta A, Fernandez-Mendez S, Enrichment and coupling of the finite element and meshless methods. *International Journal for Numerical Methods in Engineering* 2000;48(11):1615–36.
- [12] Wagner GJ, Liu WK. Application of essential boundary conditions in mesh-free methods: a corrected collection method. *International Journal for Numerical Methods in Engineering* 2000;47:1367–79.
- [13] Huerta A, Fernández-Méndez S, Liu WKA. Comparison of two formulations to blend finite elements and mesh-free methods. *Computer Methods in Applied Mechanics and Engineering* 2004;193:1105–17.
- [14] Chen JS, Wang H-P. New boundary condition treatments in meshfree computation of contact problems. *Computer Methods in Applied Mechanics and Engineering* 2000;187:441–68.
- [15] Chen JS, Wu CT, Yoon S, You Y. A stabilized conforming nodal integration for Galerkin meshfree methods. *International Journal for Numerical Methods in Engineering* 2001;50:439–66.
- [16] Chen JS, Yoon S, Wu CT. Nonlinear version of stabilized conforming nodal integration for Galerkin meshfree methods. *International Journal for Numerical Methods in Engineering* 2002;52:2587–615.
- [17] Rabczuk T, Belytschko T, Xiao SP. Stable particle methods based on Lagrangian kernels. *Computer Methods in Applied Mechanics and Engineering* 2004;193:1035–63.
- [18] Rabczuk T, Xiao SP, Sauer M. Coupling of meshfree methods with finite elements: Basic concepts and test results. *Communications in Numerical Methods in Engineering* 2006;22:1031–65.
- [19] Puso MA, Chen JS, Zywicz E, Elmer W. Meshfree and finite element nodal integration methods. *International Journal for Numerical Methods in Engineering* 2008;74:416–46.
- [20] Karutz H, Kraetzig W. A quadtree data structure for the coupled finite-element/element-free Galerkin method. *International Journal for Numerical Methods in Engineering* 2002;375–91.
- [21] Liu GR. *Mesh free methods*. CRC Press, ISBN 0-8493-1238-8; 2002.
- [22] Belytschko T, Guo Y, Liu WK, Xiao SP. A unified stability analysis of meshless particle methods. *International Journal for Numerical Methods in Engineering* 2000;48:1359–400.
- [23] Timoshenko SP, Goodier JN. *Theory of elasticity*. 3rd ed. New York: McGraw-Hill; 1970.
- [24] Zhou Q, Mayer B. Characterization of aluminum honeycomb material failure in large deformation compression, shear, and tearing. *Journal of Engineering Materials and Technology* 2002;124:412–20.